Research Article

Metamaterial-Loaded 16-Printed Log Periodic Antenna Array for Microwave Imaging of Breast Tumor Detection

Avez Syed [ID],[1] Muntasir Sheikh,[1] Mohammad Tariqul Islam,[2] and Hatem Rmili [ID][1,3]

[1]*Electrical and Computer Engineering Department, Faculty of Engineering, King Abdulaziz University, P.O. Box 80204, Jeddah 21589, Saudi Arabia*
[2]*Faculty of Engineering and Built Environment, Universiti Kebangsaan Malaysia, Bangi 43600, Selangor, Malaysia*
[3]*K. A. CARE Energy Research and Innovation Center, King Abdulaziz University, Jeddah, Saudi Arabia*

Correspondence should be addressed to Hatem Rmili; hmrmili@kau.edu.sa

This article presents printed log periodic antennas with metamaterials for use in microwave imaging. A single layer of epsilon negative (ENG) metamaterial (MTM) array (1×6) of the unit cell is on the radiating patch. Adding a single negative metamaterial structure enhances the properties of far-field antennas, such as radiation pattern and gain, both of which are vital for breast imaging. Two frequency bands exhibit negative permittivity: 3–3.3 GHz and 3.6–4.5 GHz. In the operating band, the proposed antennas have achieved a maximum gain of 5.5 dBi and impedance bandwidth of 3 GHz (2–5 GHz) with a reflection coefficient less than −10 dB. At the lowest operating frequency of 2 GHz, the electrical dimensions of this designed antenna are $0.34\lambda \times 0.26\lambda \times 0.01\lambda$. All 16 transceiver antennas are arranged vertically in a circular pattern around the phantom, each acting as a transmitter and the rest as receivers. The system design is carried out with the electromagnetic simulators CST and HFSS. After receiving the extracted data, the data are postprocessed using the MATLAB software and the delay multiply and sum (DMAS) imaging algorithm. Based on the reconstructed image, it is evident that the MTM-loaded antenna-based imaging system can detect many undesired tumors inside the breast phantom.

1. Introduction

Cells in the human body divide, stay connected, and function properly. When this cycle of division is disrupted, tumors and lumps form. When the latter attack other nearby organic tissues, they develop into dangerous tumors, also known as disease-indicating metastasis [1]. Cancer is a significant public health problem that needs to be detected in its early stages. It is considered the leading cause of death. Early cancer revelation and treatment can result in a 97 per cent survival rate, highlighting the critical need for reliable and efficient methods for early tumor detection. The interaction of electromagnetic or acoustic waves with body tissues and fluids underpins the majority of clinical imaging tests today, but they all do not function in the desired frequency band [2]. Among the various categories of clinical image analysis, X-rays are the most commonly used as they

provide more reliable diagnostic results. X-rays are high-energy electromagnetic radiation, although ionizing radiation has been shown to have some beneficial uses in humans, it can have adverse effects even when used as a diagnostic test [3]. Radiation interactions with cells are stochastic functions, that is, there may or may not be an interaction, and damage may or may not occur when an interaction occurs. As a result, using it in biological testing raises the chances of causing irreversible cell alterations, resulting in cell mutation and death [4].

For the reasons stated above, considerable efforts have been made in recent years to develop a viable cancer diagnostic tool that does not require the utilization of ionization radiation. Some microwave signal processing techniques based on image reconstruction methods have been investigated [5–10]. Microwave imaging, unlike X-rays, can be done more frequently since it is nonionizing. Low

cost, low complexity, high data rate, low power spectral density, high accuracy range, and noninvasiveness are all advantages of microwave imaging systems. One of the most promising candidates is the microwave imaging system (MIS) based on ultrawideband (UWB) radiation with a span of frequencies varying from 3.1 to 10.6 GHz [11]. With the recent advances in hardware and software, the microwave imaging technique has gained much interest due to its low cost and nonionizing characteristics.

In recent decades, several UWB antennas for the MIS have been proposed, including the slotted antennas [12–14], dipole antenna [15], Vivaldi antennas [16–18], Vee dipole [19], tunable antenna [20], and resistively loaded bowtie antenna [21]. Performance of these sensor elements needs to be improved to provide a higher degree of resolution and detection. Literature cites a wide range of techniques such as electromagnetic bandgap (EBG) [22], meta-surfaces [23], superstructures [24], split ring resonators (SRRs) [25], co-planar waveguide (CPW) [26], metalens [27], and frequency selective surface (FSS) [28], which improve gain, coupling, and bandwidth of the antenna. The MIS is found to be effective in detecting breast cancers in a variety of simulations and experiments.

In the study by Imani et al. [23], a one-port dynamic metasurface aperture can generate various illumination patterns at microwave frequencies. The system consists of a cavity, with the upper surface of the conduction modelled with metamaterial elements. Numerical simulations show how the device works in computational microwave imaging. However, the permeability or permittivity characteristics of the metamaterial was not presented. The complex design covers significantly less impedance bandwidth without including the UWB range. Besides, the imaging process is not clearly described. An array of multifrequency dipole antennas is explored for microwave imaging in the study by Saenz et al. [24]. Over the array, a superstrate is applied to reduce the coupling between the dipoles. Analyzing the fields radiated by the antennas and determining the far-field measurements of the antennas, the superstrate is observed to limit the radiated power, boost boresight radiation, and decrease end-fire radiation. Nevertheless, the properties of the metasurface used are not described. The design in the article works in the higher frequencies but fails to cover the lower frequencies. The authors in this study [24], describe the antenna system for imaging but fail to present the reconstructed images.

The design of an SRR sensor for microwave applications is described in the study by Mukherjee et al. [25]. For interrogating composites via edge coupling, a modified sensor design is used. Using the band-stop design, several cells of different sizes are incorporated into an array. Each cell resonates at a separate frequency, allowing for dynamic tuning characteristics such as a high Q factor, low-frequency penetration, and high-frequency resolution. Furthermore, the sensor includes a built-in reference resonator, which avoids the requirement for a calibration procedure. The sensor antenna is compact in size and operates in the 6–12 GHz frequency band. However, the reconstructed images are noisy in this study [25], and hence, need to

modify or develop an algorithm to eliminate the effect of noise in the reconstructed images. In the study by Zhang et al. [27], the proposal for independent manipulation of the right- and left-hand circularly polarized waves is made for bifunctional metalens constructed with metaatoms. Two independent features in all these metalenses can be switched by switching on the helicity of the illumination. The ultrathin metasurface of $0.15\lambda 0$ thickness achieves very high efficiencies of approximately 80 per cent, with a peak value of 91 per cent. In this case, the design structure is complex, and the size is not compact. Also, its purpose for imaging is not clear. In the study by Abdulhasan et al. [28], UWB FSS was miniatured to enhance the UWB antenna gain for the application of microwave imaging. The FSS unit cell is created by fusing a square loop and a cross-dipole on an FR4 substrate. A good improvement of 3.5 dBi gain, unidirectional, and bandwidth of 3.8–10.6 GHz is achieved through the antenna prototype. However, the antenna fails to operate in the lower frequencies. The Image displayed by the system was higher in resolution than the image displayed by the antenna without FSS. But the structure is complex to implement in the portable imaging system.

In this paper, a modified, printed log periodic antenna (PLPA) with metamaterial loaded is designed and is used for microwave imaging applications for breast cancer detection. Initially, a CPW-fed sensor element loaded with a 1×6 array of metamaterial unit cells is designed and later extended to a 16-element circular array. The performance of the PLPA is enhanced and is used as a transceiver in the breast tumor detection system. Finally, the collected backscattered signals are postprocessed using MATLAB to locate the tumor in the breast phantom.

2. Antenna Design

The PLPA structure was first developed in the antenna design, followed by the creation of metamaterial unit cells. The main target is integrating the PLPA with a 1×6 metamaterial unit cell array.

2.1. Unit Cell Design.
A novel design view of the printed planar metamaterial unit cell is shown in Figure 1(a). It consists of three-square copper strips with a thickness of 0.035 mm. The structure is planar and compact with the dimension of $(a \times b)$ mm^2. The inner gap between the square strip patches is $d = 0.3$ mm. The designed unit cell is fabricated on a 6 mm × 6 mm FR4 substrate with a permittivity of 4.4, a thickness of 1.6 mm and a loss tangent of 0.02. A vertical magnetic field is induced in the square strip rings, which often leads to negative permittivity. The resonance is controlled by the gap in strips and the long horizontal copper strip moving across all three-square strips. The metal strip represents inductance while the split in the metal strip loop forms capacitance. An important goal of the unit cell is to attain resonance within the range of 2–5 GHz for microwave imaging of breast cancer. The simulations are performed by the CST microwave studio to analyze the parameters. The unit cell design is positioned within the two
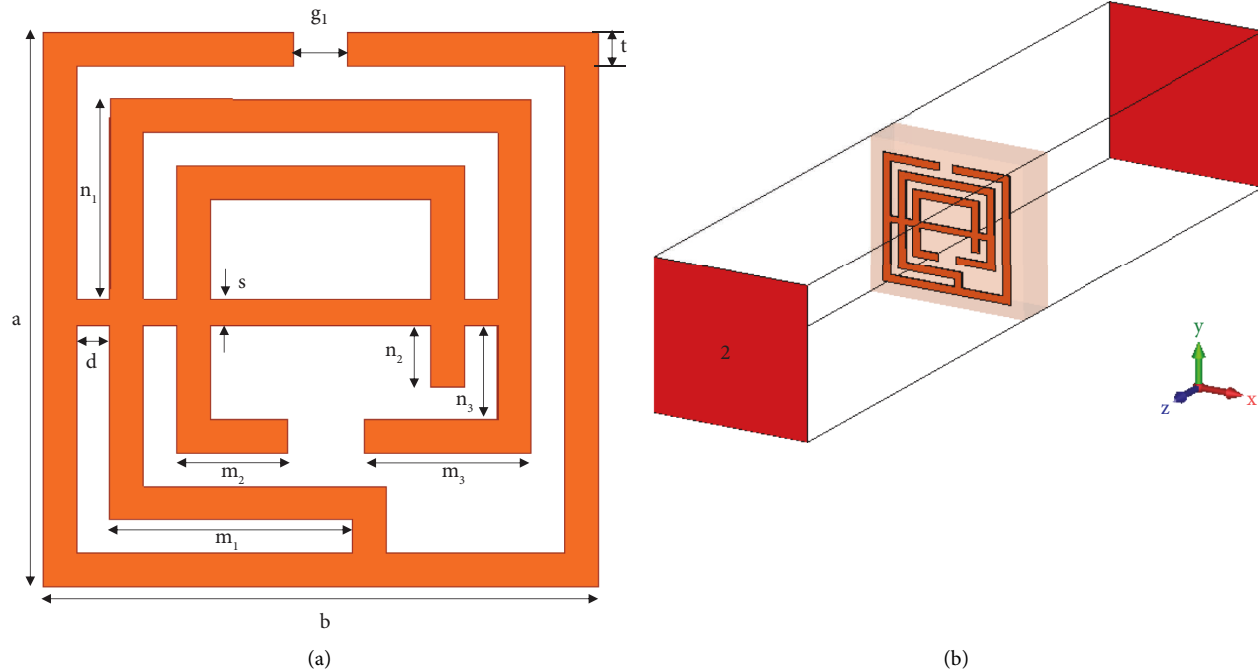
FIGURE 1: The MTM unit cell structure (a) schematic layout and (b) CST simulation setup.

waveguide ports on the positive and negative Z-axes, as illustrated in Figure 1(b). Boundary conditions are defined as electric field on X-axis, magnetic field on Y-axis, and open space on Z-axis. The design parameters are optimized as follows: $a = 5$ mm, $b = 5$ mm, $d = 0.3$ mm, $s = 0.25$ mm, $t = 0.3$ mm, $g_1 = 0.5$ mm, $m_1 = 2.2$ mm, $m_2 = 1$ mm, $m_3 = 1.5$ mm, $n_1 = 1.8$ mm, $n_2 = 0.55$ mm, and $n_3 = 0.85$ mm.

The proposed unit cell structure is constructed in various design stages, as shown in Figure 2. All the three-square ring resonators have a width of 0.3 mm, and the gap between every resonator is also 0.3 mm. The reflection (S11) and transmission (S21) coefficients of the proposed unit cell are shown in Figure 3. Initial design1 consists of two-square ring resonators; however, it does not meet the −10 dB threshold for S-parameters in the 2–5 GHz band. A long horizontal strip in the inner ring is added to design 2. Although it produces resonance in the required band, its results must be improved. The structure is further modified as design 3, resulting in better return loss (−23 dB) and lower transmission coefficient (−14 dB). The proposed structure is a modification of design 3 with the inclusion of an inner square ring. A good reflection (−23 dB) and transmission coefficient (−20 dB) is achieved within the operating band.

Figure 4 presents different metamaterial parameter results of the proposed unit cell. The S-parameters of the unit cell is shown in Figure 4(a). The reflection and transmission coefficients are achieved at 4.1 GHz and 3.8 GHz, respectively. Figures 4(b), 4(c), and 4(d) represent the extracted parameters, permittivity, permeability, and refractive index, respectively. Negative permittivity is observed in two bands, 3–3.3 GHz and 3.6–4.5 GHz, while permeability approaches zero in the lower band and exceeds zero in the upper band. As a result of its properties at the operating band of the

metamaterial structure, it can be considered as a single negative characteristic, i.e., epsilon negative (ENG).

The surface current distribution on the unit cell at 3.8 GHz is shown in Figure 5. The currents are more prominent within the right half of the outer square ring and around the lower portion of the inner rings. However, the current distribution is nonuniform throughout the unit cell due to modified square ring structures. There is an opposite current flow around the square rings within concentrated currents, and the outer ring has an opposing current to the inner ring, creating the stop band.

2.2. Metamaterial-Loaded PLPA. The PLPA patch antenna is modified by adding the MTM unit cells. Due to its negative properties, MTM enhances the performance of antennas by controlling electromagnetic waves. In the end-fire direction, an array of 1×6 unit cells are arranged on the radiating patch, with a spacing of 1.6 mm between the cells. Design and fabrication of the antenna prototype are carried out on an FR4 substrate with a permittivity of 4.4, a thickness of 1.6 mm and loss tangent of 0.02. This prototyping format has a dimension of 50 mm × 40 mm, making it planar and compact. The antenna structure is shown in Figure 6. The color orange represents the patch, and the peach color represents the FR4 substrate. As a substrate, FR4 is preferred due to its affordability, ease of access, fabrication simplicity, and versatility. SMA connectors are used to feed the design patch over 50 Ω CPW feedline. CPW feedlines are well suited to wide bandwidth requirements, better matching, easier integration, and lower dispersion. The proposed antenna with MTM cover a frequency band between 2 GHz and 5 GHz. By integrating MTM, antenna performance is
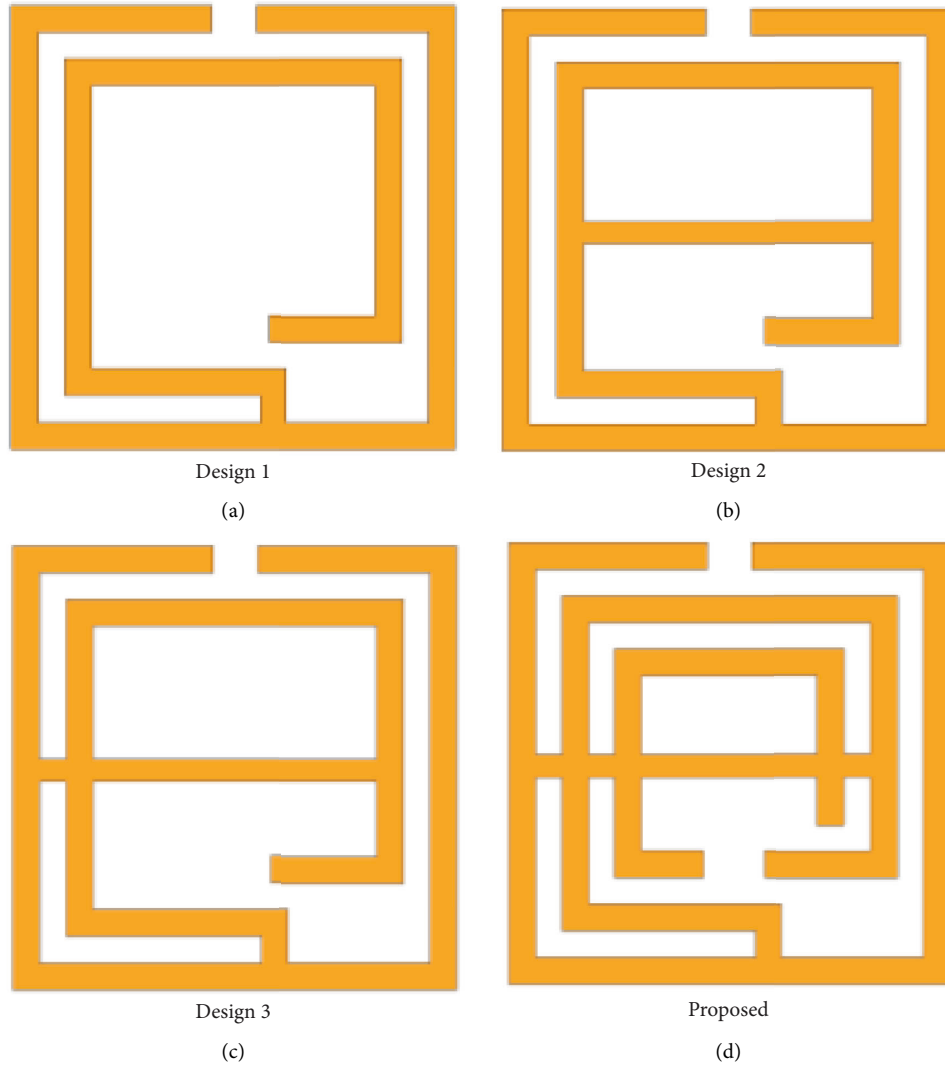
Design 1

(a)

Design 2

(b)

Design 3

(c)

Proposed

(d)

FIGURE 2: Different design stages of MTM unit cell structure. (a) Design 1 (b) design 2 (c) design 3 (d) proposed.
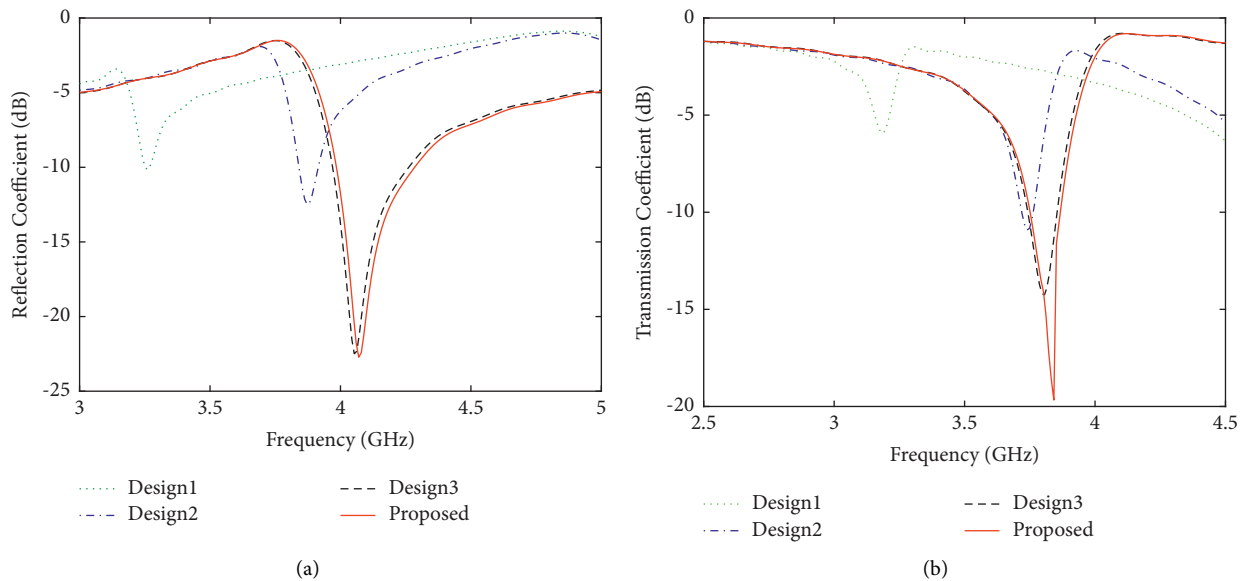

(a)

(b)

FIGURE 3: Parametric analysis of the proposed MTM unit cell; (a) reflection coefficient and (b) transmission coefficient.
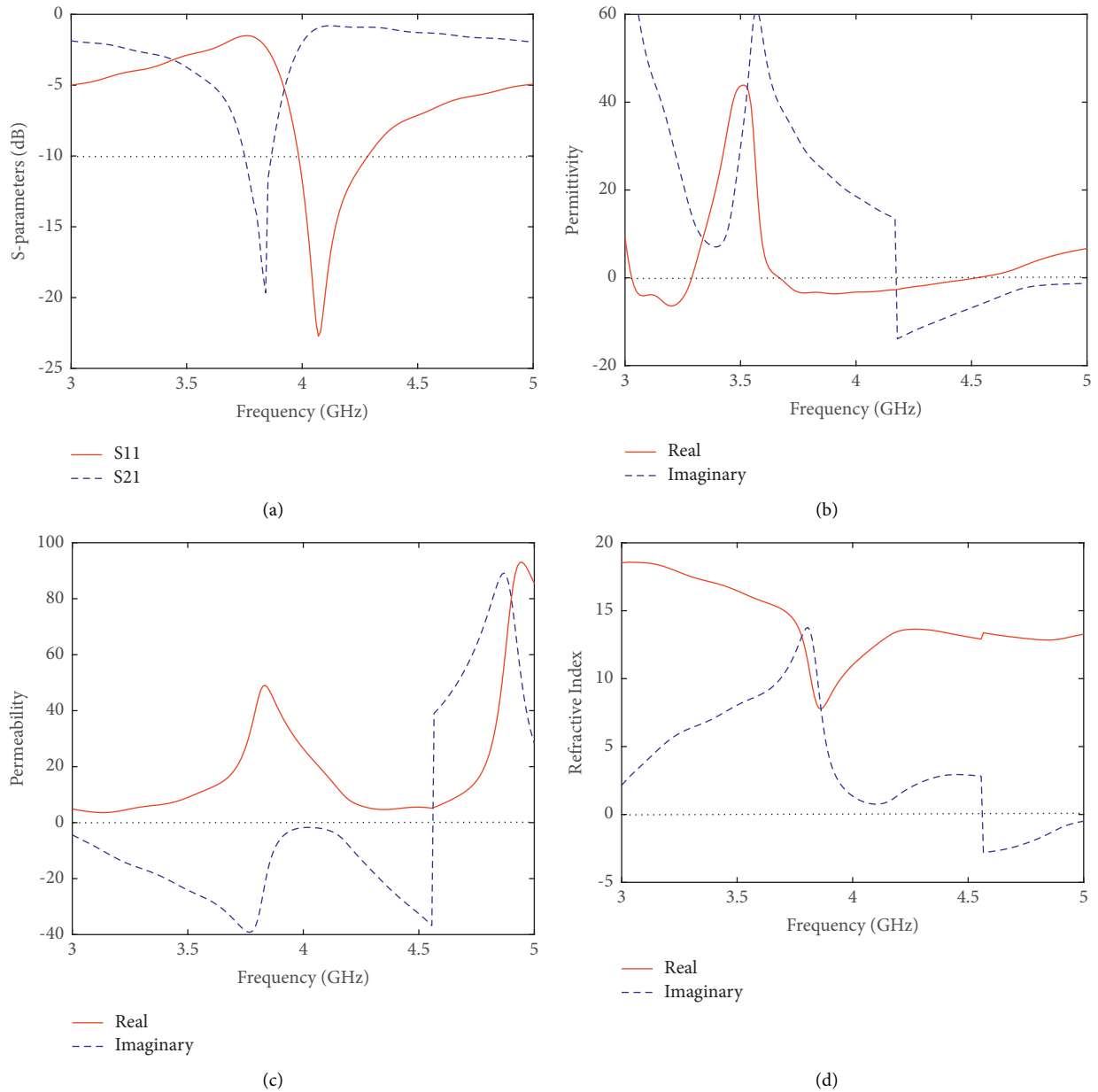
(a)

(b)

(c)

(d)

FIGURE 4: Proposed unit cell structure (a) S-parameters, (b) permittivity, (c) permeability, and (d) refractive index.

enhanced without changing the frequency bandwidth. The antenna dipoles, MTM unit cells, and the feedline are printed on one side of the substrate in a single step so that a simplified single-printed layer is formed. The FR4 substrate is arrayed with five dipole elements along a strip transmission line connected to the 50 Ω feedline.

3. Parametric Study

In order to optimize the performance of the antenna based on the larger dipole, w_1 and w_6 parameters are optimized,

and HFSS simulation software is used to perform the parametric analysis.

3.1. The Effect of the Length w_1. Figure 7 illustrates how w_1 affects the performance of the PLPA in terms of bandwidth. With all other parameters remaining the same, the value of w_1 is increased by 1 mm from 10.5 mm to 13.5 mm. A poor match can be found for the lengths of 10.5 mm and 13.5 mm at 3 GHz. Compared to 11.5 mm, 12.5 mm does not improve the return loss. Therefore, w_1 is optimal at 11.5 mm, which provides superior match and return loss characteristics. A
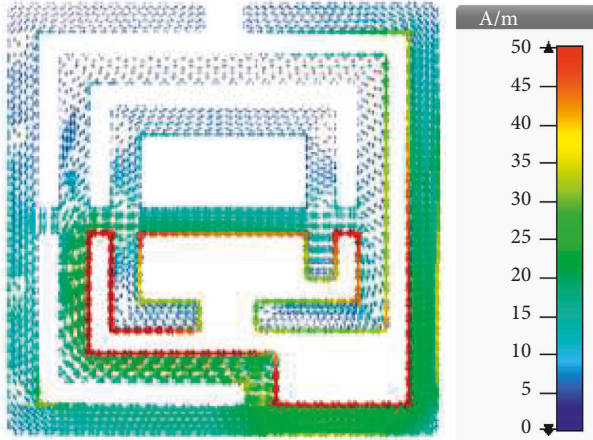
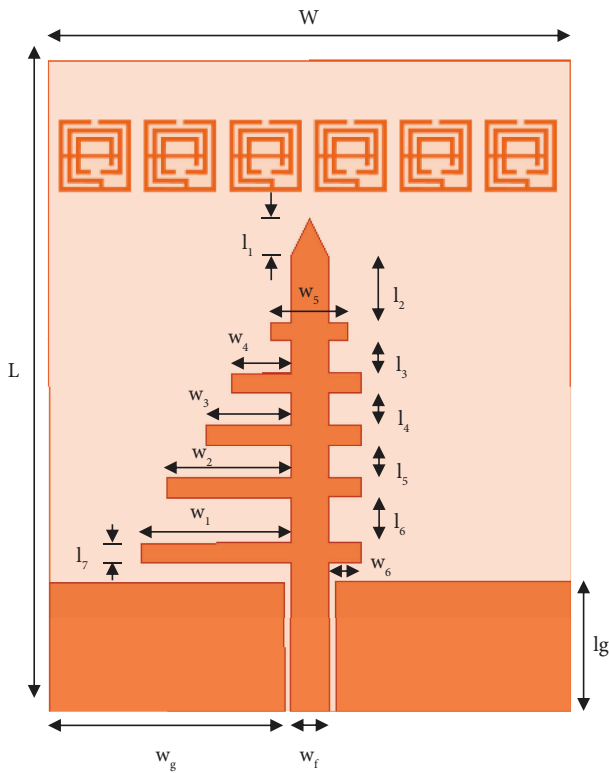FIGURE 5: Surface current distribution on unit cell at 3.8 GHz.

FIGURE 7: Variation of return loss versus frequency at different values of w_1[29].

FIGURE 6: Geometrical dimensions of the proposed PLPA.
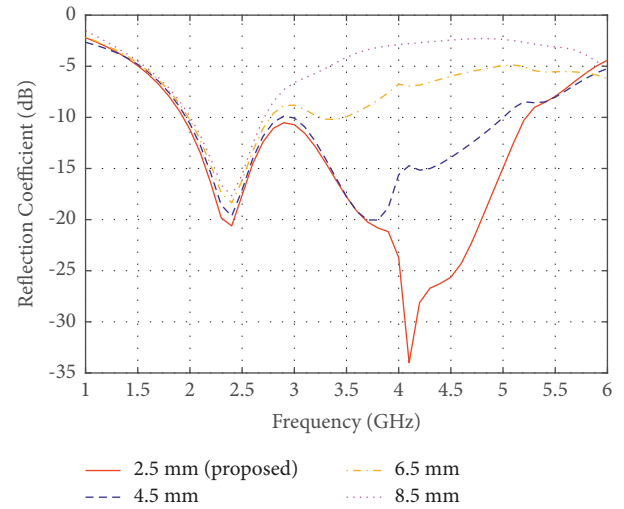
FIGURE 8: Variation of return loss versus frequency at different values of w_6[29].

reflection coefficient of −20 dB is found at lower resonant frequencies, but −35 dB is found at higher resonant frequencies.

3.2. The Effect of the Length w_6. Figure 8 shows the effect of the w_6 variation on the reflection coefficient. In this case, w_1 is set at 11.5 mm. As the value of w_6 increases by 2 mm, it goes from 2.5 to 8.5 mm. In contrast to the lower resonant
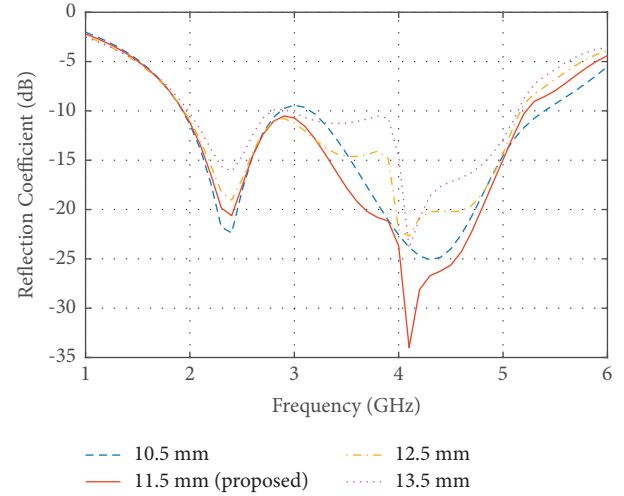
frequency, the higher one depends on w_6. Therefore, the tuning factor comes into play, where each dimension (one factor) is considered individually. In the interval between 2.5 mm and 8.5 mm, the higher resonant degrade until it is completely lost. Consequently, 2.5 mm becomes the final optimized w_6 value. The structural parameters of the proposed PLPA antenna are initially determined by the modified Carrel method [30], and later the process of optimization is carried out.

In terms of structural dimensions, the PLPA is optimized as follows: $L = 50$ mm, $W = 40$ mm, $w_f = 3$ mm, $w_g = 18$ mm, $l_g = 10$ mm, $l_1 = 3$ mm, $l_2 = 5$ mm, $l_3 = 2.5$ mm, $l_4 = 2.5$ mm, $l_5 = 2.5$ mm, $l_6 = 3.5$ mm, $l_7 = 1.5$ mm, $w_1 = 11.5$ mm, $w_2 = 9.5$ mm, $w_3 = 6.5$ mm, $w_4 = 4.5$ mm, $w_5 = 6$ mm, and $w_6 = 2.5$ mm. This prototype is intended to act as a sensor in an array for the MIS in order to detect breast cancer. For the MIS, a large bandwidth, high gain, and stable directional radiation pattern are vital.
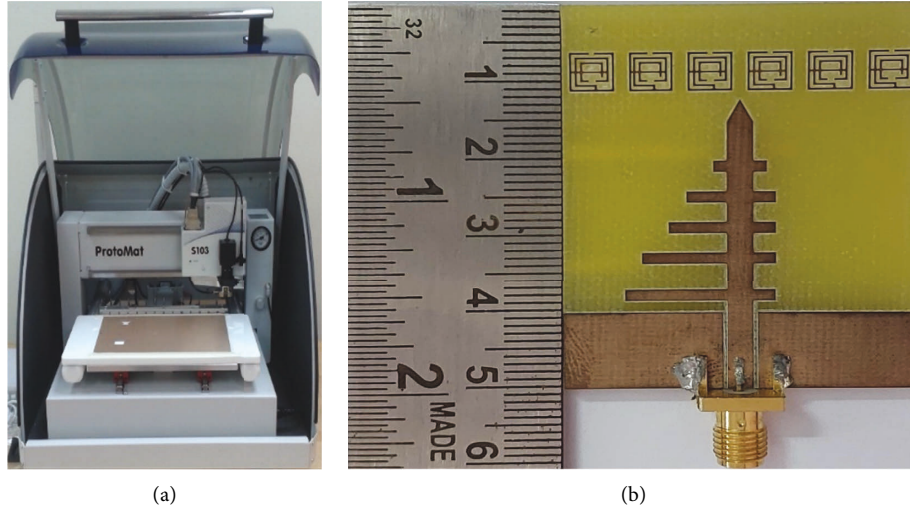
FIGURE 9: (a) The LPKF (S103) protoMat machine and (b) The PLPA antenna prototype.

4. Analysis and Discussion

LPKF protoMat (S103) circuit board plotters were used to design the antenna prototype, and a Tektronix USB vector network analyzer (TTR506A) was used to evaluate its performance. Figure 9 depicts an experimental prototype of the antenna. It appears that the simulated and measured return loss for the antenna design with and without MTM, as shown in Figure 10, is in good agreement. As can be seen, the bandwidth characteristics of the PLPA are not impacted much by the installation of MTM. According to the measurement results, the antenna operates between 2 and 5 GHz (−10 dB criteria). It is mainly the SMA connector, cables, and fabrication tolerance that cause the slight appearance of a deviation between the simulation and experimental results. The characteristics thus obtained aid the PLPA in its role as a sensor in the MIS.

Furthermore, to understand the performance of the loaded antenna, the surface current density on the antenna at 3.5 GHz and 5 GHz is shown in Figure 11. A directional radiation pattern is seen at 3.5 GHz due to the strong concentration of current on the large dipole, around the outer ring of all unit cells, and the transmission strip line. Similarly, higher frequencies of 5 GHz show a similar distribution of current. As a result, a directed pattern appears across the whole radiating patch, with high density concentrated around large and adjacent dipoles.

According to the following equations [29], the length of the large dipole element (L_{dipole}) can be determined as follows:

$$L_{\text{dipole}} = [\text{w1} + \text{wf} + \text{w6}] \approx \frac{c}{2f_H\sqrt{\varepsilon_{eff}}}, \quad (1)$$

$$\varepsilon_{eff} = \frac{\varepsilon_r + 1}{2} + \frac{\varepsilon_r + 1}{2}\frac{1}{\sqrt{1 + 12h/l_7}}, \quad (2)$$
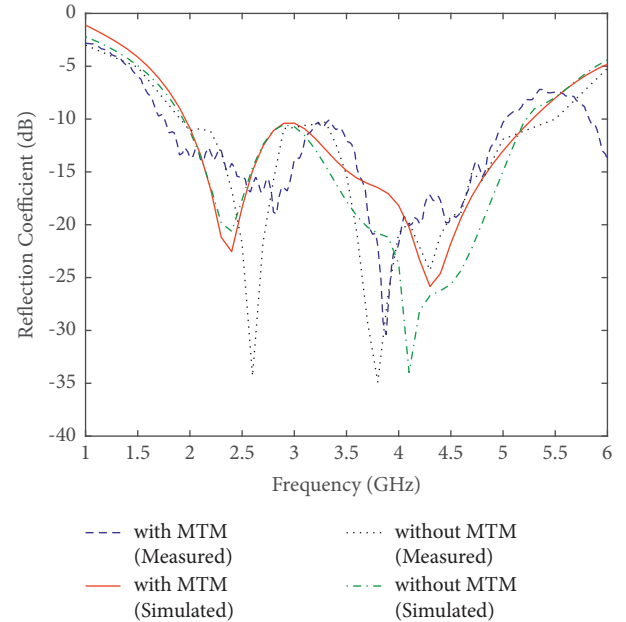

FIGURE 10: Simulated and measured reflection coefficient curves with and without MTM.

where $c = 3 \times 10^8$ m/s, ε_{eff} is the effective permittivity, ε_r is the substrate dielectric constant, h is the height of substrate, l_7 is the width of the dipole element (all dipoles are of equal width), and f_H is the highest frequency in the operating band. As determined by equation (1), the theoretical length of the larger dipole element is 16.2 mm, and its practical length is 17 mm.

The 2D and 3D radiation patterns of the prototype for two nonidentical frequencies of 3.5 and 5 GHz are plotted in Figure 12 to clarify the antenna radiation performance. The 2D patterns at both the frequencies are taken from the XZ plane ($\phi = 0°$ plane). As observed from Figure 12, the
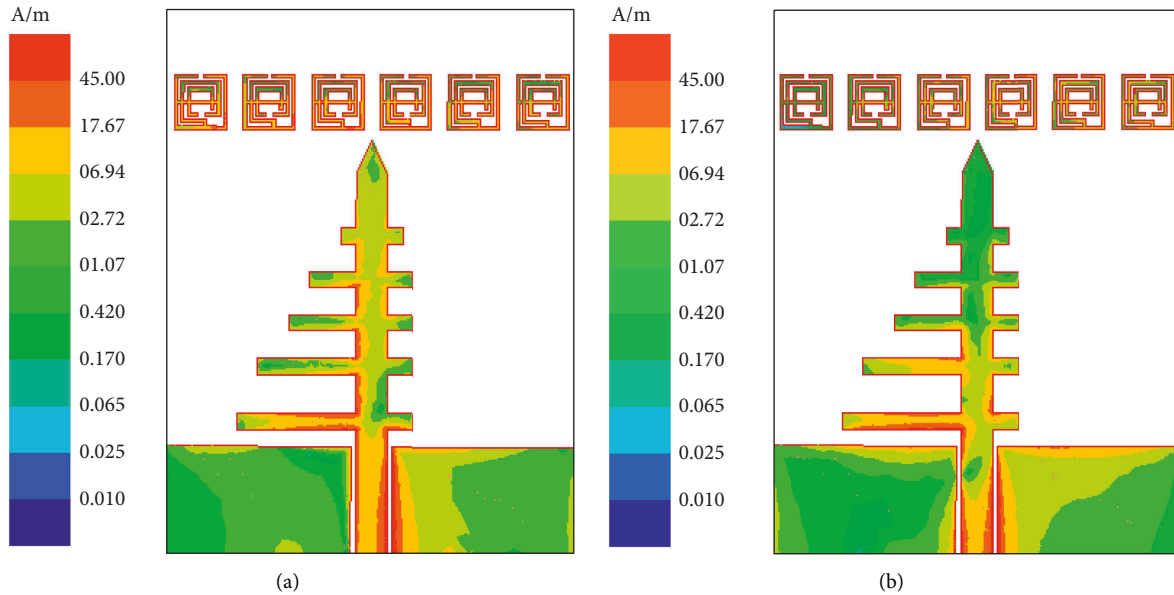
FIGURE 11: Surface current distribution on the PLPA at (a) 3.5 GHz and (b) 5 GHz.

proposed antenna is directional, with the main radiator patch oriented toward the boresight. On the operational band, the major lobes of the patterns point in the direction of the end-fire. Figure 13 shows the gain curve for the prototype with and without MTM. It has been discovered that with the addition of MTM structures, the gain has increased at a significant rate without compromising the bandwidth. From 2–5 GHz, the CPW-fed PLPA covers a bandwidth of 3 GHz (−10 dB criteria) with a peak gain of 5.5 dBi.

5. Microwave Imaging System

An overview of the architecture and various components of the proposed breast imaging system is shown in Figure 14. An antenna array is proposed for microwave imaging, which includes 16 antennas (one for transmitting and fifteen for receiving ultrawideband signals), a stepper motor mount for the antennas, a switching system for controlling the receivers, and a personal computer for signal processing and image reconstruction. It shows the 16-antenna array being tested for its ability to detect breast tumors using CST and HFSS simulation software, with a breast phantom as a test piece. Antenna arrays can be rotated using steppers around the breast phantom in polar coordinates from 0 to 2π. Low-loss coaxial cables connect the 16 antennas to a control switching network. Switching the receiving antennas collects the received signal from all fifteen receivers. The data (switching matrix) is collected and postprocessed using MATLAB. The imaging system uses a Tektronix USB vector network analyzer (VNA, TTR506A) microwave transceiver. Microwave signals are generated by port 1 of the VNA and transmitted to the breast phantom through the transmitting antenna. The remaining fifteen antennas transmit the

received backscattered signal to the image-processing unit after being picked up by another port on the switching system. All these devices and electromechanical circuits related to the data acquisition process are connected to the personal computer (PC) through the USB port. In addition, the VNA is connected to a PC, which receives data for further processing. Using MATLAB, the collected data are processed using the delay multiply and sum (DMAS) imaging algorithm to locate and detect tumors inside the breast.

The phantom used is composed of layers of skin and fat tissue with a tumor inserted. With an air gap of 15 mm, the antenna array is placed closely around the breast phantom in a circular pattern of a radius of 60 mm. It means there is no direct contact between the antenna array and the breast phantom. The dielectric constant of the skin, fat, and tumor are 38, 5.14, and 67, respectively. The imaging is performed with two phantoms, one with a single tumor and the other with two tumors. A single cylindrical tumor with a radius of 5 mm and a height of 20 mm is inserted in the first phantom. The second phantom is made more challenging by adding two identical cylindrical tumors on the opposite side of the center. Approximately, 8 cm separates the antennas from the center of the phantom. There is a 22.5 degree spacing between the array elements, which results in transmission coefficients below −15 dB when the breast phantom is present. When a phantom with a single tumor is employed, the antenna array exhibits reflection and transmission coefficients of less than −10 dB over a bandwidth of 2 to 5 GHz, as illustrated in Figure 15. With two tumors, the array exhibits coefficients less than −15 dB over a frequency range of 2 to 5 GHz, as shown in Figure 16.
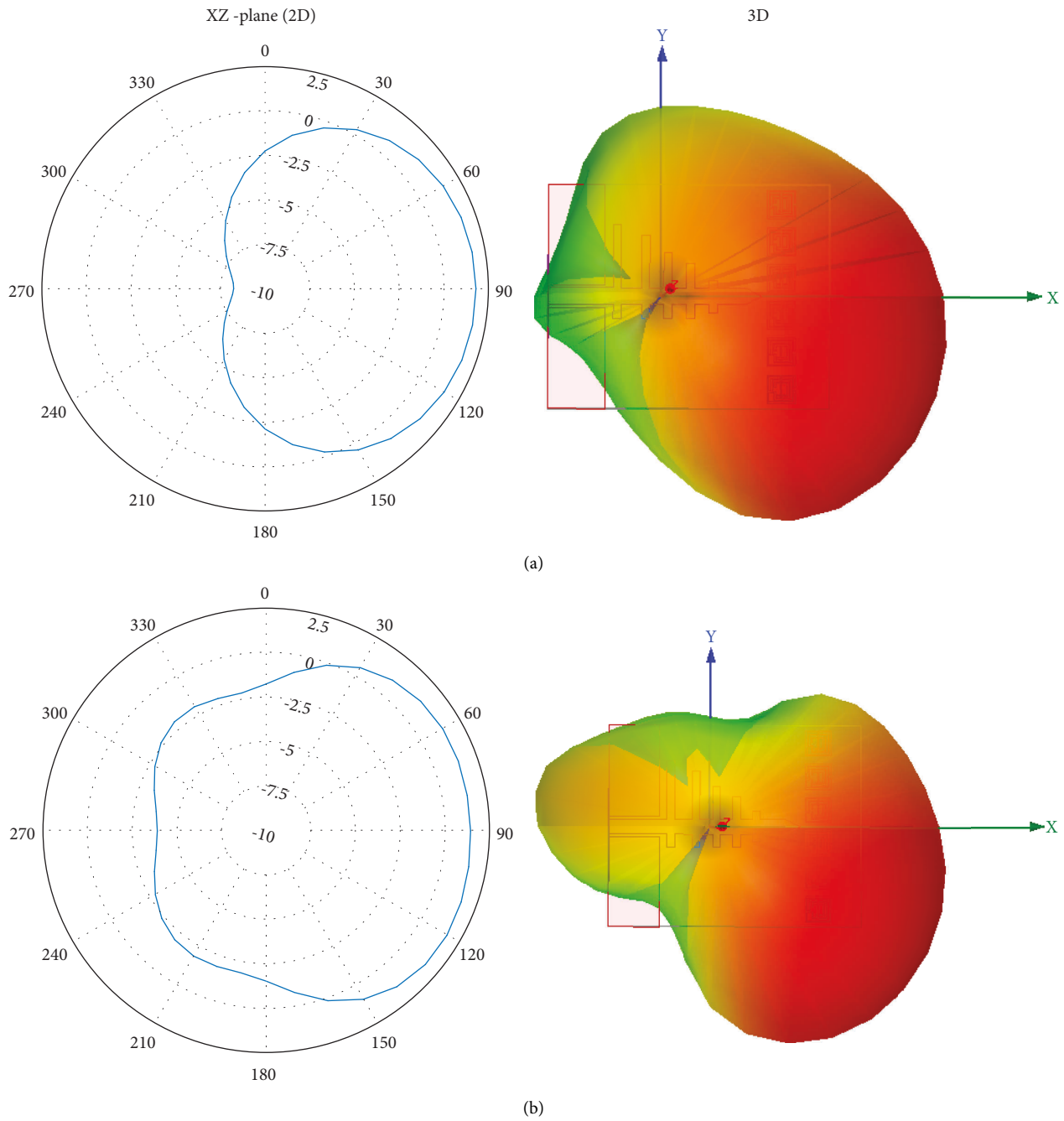
XZ -plane (2D)

3D

(a)

(b)

Figure 12: Radiation patterns of the PLPA in 2D and 3D at (a) 3.5 GHz and (b) 5 GHz.

In the proposed MIS, 16 antennas are used; one is a transmitter, whereas the remaining 15 are receivers that gather scattered signals from the phantom. The antenna switching process is programmatically controlled in the simulation environment. Many scattered signals as a dataset are needed to generate a high-resolution image. A total of 240 (16×15) scanned data points are obtained from the breast phantom after repeating the whole procedure for all antennas. After that, the collected data are postprocessed by the DMAS algorithm [31] and DAS algorithm [32] for
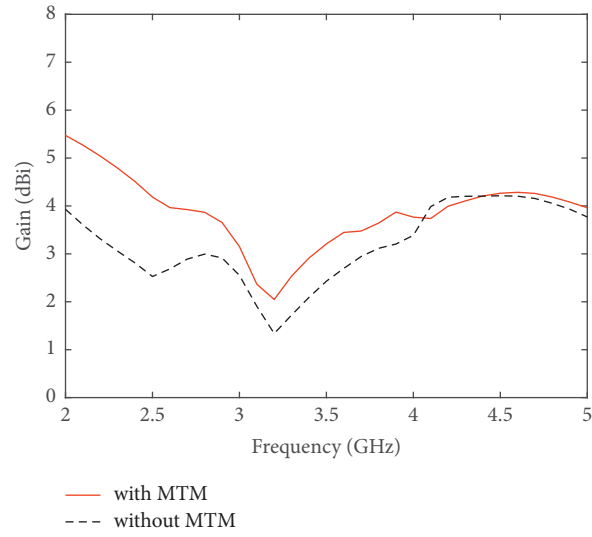
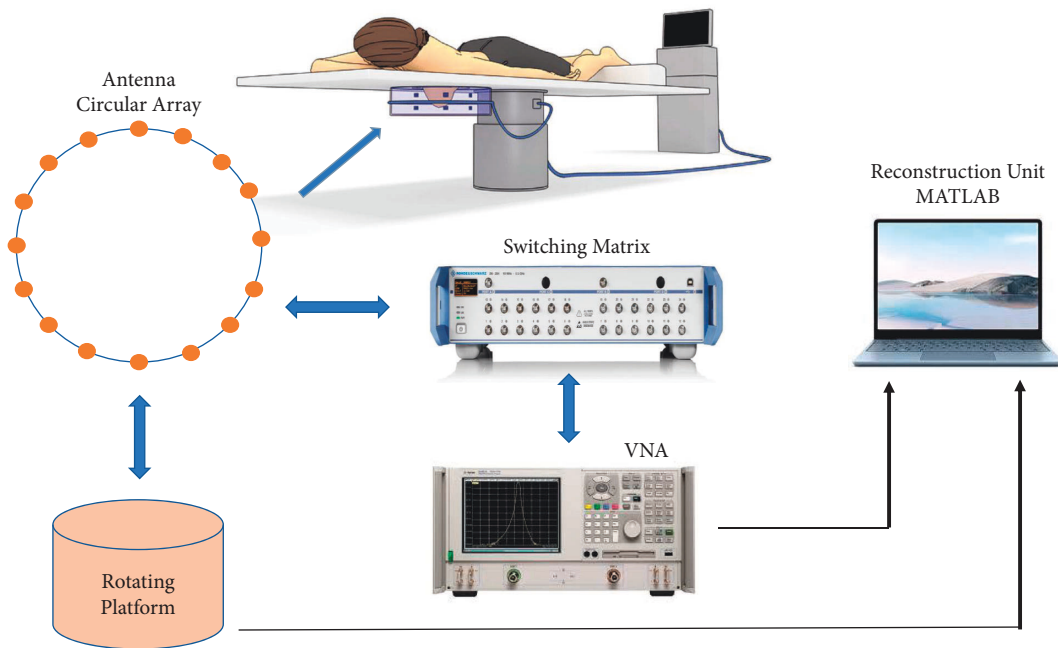FIGURE 13: Peak gain of the proposed PLPA antenna with and without MTM.

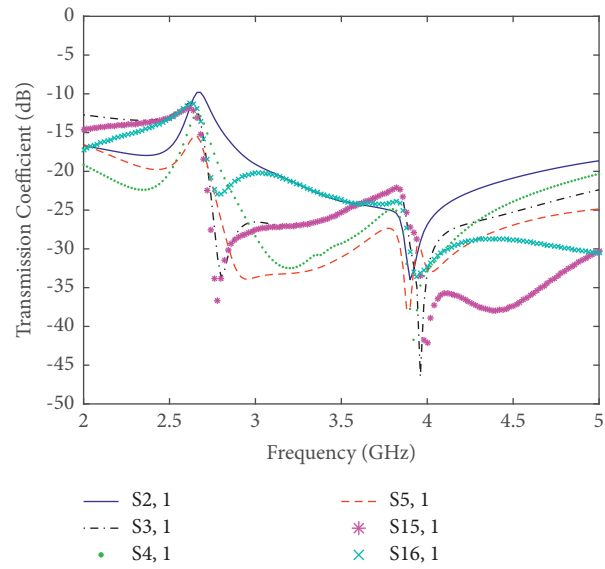FIGURE 14: Setup of microwave imaging system.

Figure 15: Scattering matrix of 16 PLPA elements around single-tumor phantom: S2, 1-S3, 1-S4, 1-S5, 1-S15, and 1-S16, 1.
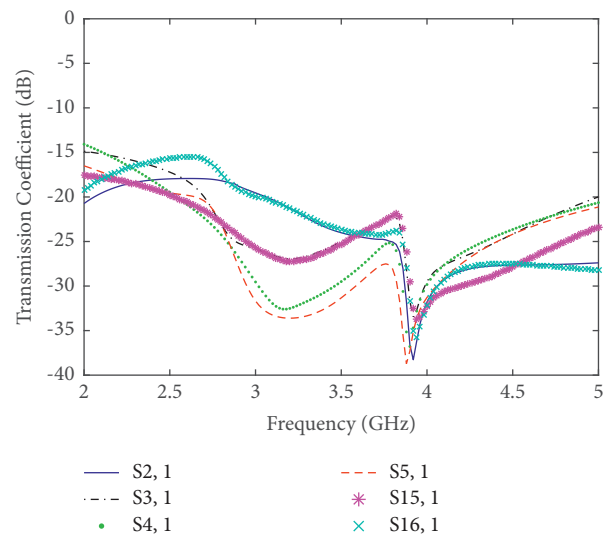

Figure 16: Scattering matrix of 16 PLPA elements around double-tumor phantom: S2, 1-S3, 1-S4, 1-S5, 1-S15, 1-S16, and 1.
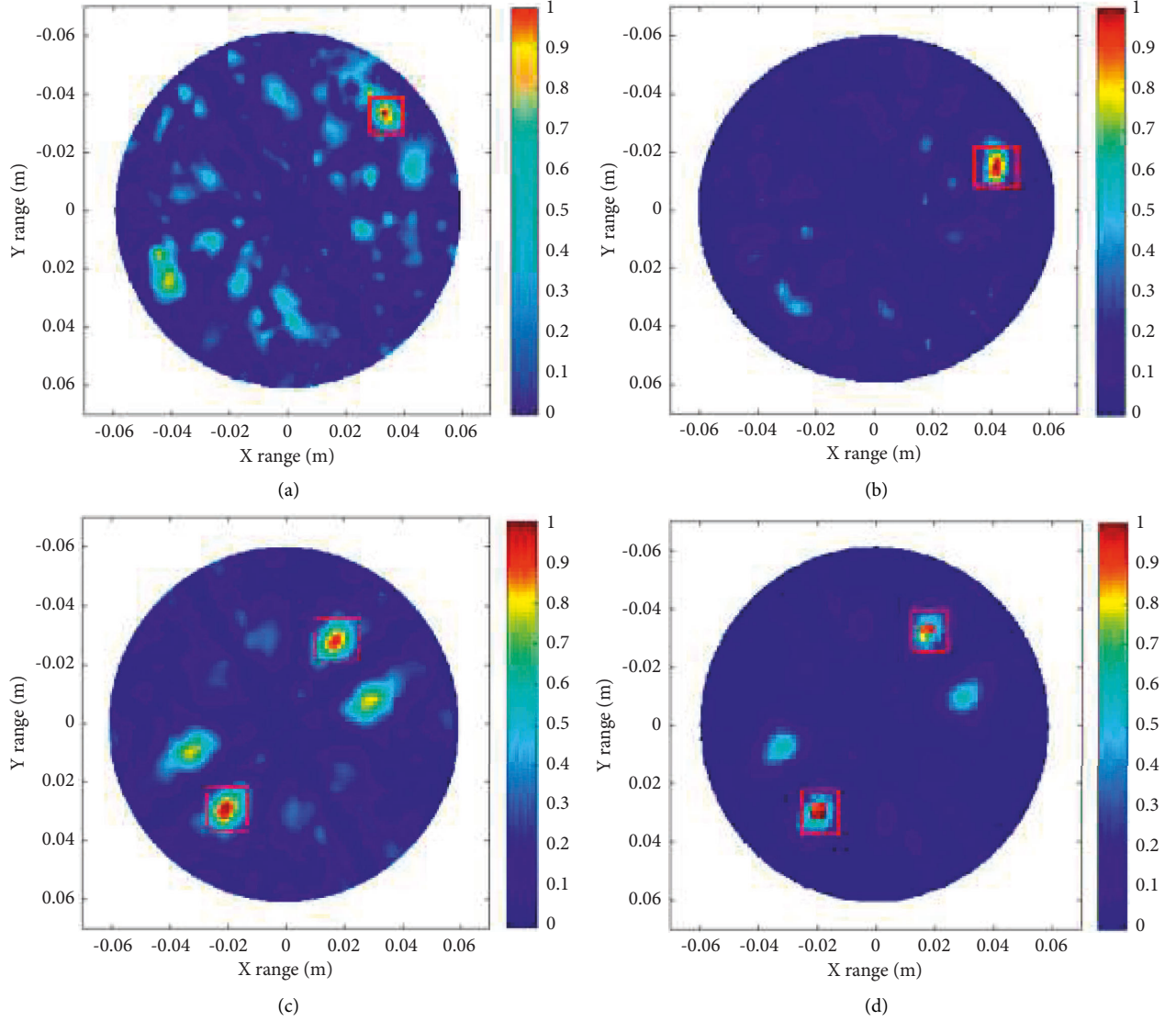
Figure 17: Reconstructed images of the tumorous breast phantom (a) single tumor (DAS), (b) single tumor (DMAS), (c) double tumor (DAS), and (d) double tumor (DMAS).

imaging purposes using MATLAB programming. The algorithm is well suited to produce high-resolution images and detect the tumor inside the breast phantom. The main formulas of these algorithms are given below:

$$\gamma_{\text{DAS}}(i) = \left(\int_{-\infty}^{\infty} \sum_{\forall \varphi_{\text{odd}}} \sum_{\forall rx} \Gamma\left(t - \frac{\tau(i, rx, \varphi_{\text{odd}})}{\Delta t}, rx, \varphi_{\text{odd}} \right) dt \right)^2,$$

$$\gamma_{\text{DMAS}}(i) = \int_{-\infty}^{\infty} \sum_{\varphi_{\text{odd}}=1}^{N/2} \sum_{tx=1}^{Tx} \sum_{rx=1}^{Rx} \sum_{\varphi'_{\text{odd}}=\varphi_{\text{odd}}}^{N/2} \sum_{tx'=tx}^{Tx} \sum_{rx'=rx+1}^{Rx} \times \left[\begin{array}{l} \Gamma\left(t - \dfrac{\tau(i, tx, rx, \varphi_{\text{odd}})}{\Delta t}, tx, rx, \varphi_{\text{odd}} \right) \times \\ \\ \Gamma\left(t - \dfrac{\tau(i, tx', rx', \varphi'_{\text{odd}})}{\Delta t}, tx', rx', \varphi'_{\text{odd}} \right) \end{array} \right] dt. \tag{3}$$

TABLE 1: Comparison of the proposed imaging system with other existing systems in the literature.

Ref	Antennas	Sizes (mm³)	Frequencies (GHz)	Gains (dBi)	Substrate	The no. of elements	Arrangements	Imaging methods
[34]	Stacked aperture coupled antenna	$37 \times 43 \times 4.85$	4.9–10.9	6.0	FR4	3	Annular	DAS
[35]	Vivaldi	$63 \times 51 \times 1$	2.5–8.5	8.5	FR4	2	Side by side	—
[36]	Lens-loaded Vivaldi	$110.3 \times 100 \times 1.6$	1–14	—	FR4	1	17 (rows) × 28 (columns) sampling locations	Inverse scattering approach
[37]	Unidirectional UWB antenna	$118 \times 76 \times 40$	2–6.5	—	FR4	2	24×16 Scanned positions	DMAS
[18]	Balanced slotted antipodal Vivaldi	$40 \times 40 \times 1.6$	3.01–11	7.1	FR4	2	Face-to-face	DMAS
[38]	Balanced antipodal Vivaldi antenna	—	1–13	—	—	1	36 positions	TSAR (tissue sensing adaptive radar)
[39]	Side-slotted Vivaldi antenna	$51 \times 42 \times 1.57$	2.8–7	7	Rogers RT/duroid 5870	9	Circular	Iteratively corrected-DAS
[40]	Planar slot UWB	$11 \times 13.1 \times 0.635$	3.1–10.6	—	RT/duroid 6010	16	4×4 crossed shaped	Confocal imaging
[41]	Vivaldi antenna	$40 \times 40 \times 1.6$	2.5–11	7.2	FR4	16	8 vertically 8 horizontally	DAS
Proposed	MTM-loaded PLPA	$50 \times 40 \times 1.6$	2–5	5.5	FR4	16	Circular	DMAS

Here, $\gamma_{DAS}(i)$ is the scattered intensity-map for the DAS algorithm, $\gamma_{DMAS}(i)$ is the scattered intensity-map for the DMAS algorithm, N represents the angular positions of each rotation, φ_{odd} = odd number of datapoints (1, 3, 5, ...$N_{\varphi-1}$), τ denotes the estimated delay time, Δt denotes the time step, and Γ denotes the data in time domain (signals converted to time domain using the inverse Fourier transform).

Using DAS and DMAS-based methods, Figure 17 shows reconstructed images of the scattered fields from the PLPA antenna array. Results are obtained by slicing along the z-axis with different horizontal planes. A DAS-based approach excels when it comes to dealing with reflections off a target tumor. By adding two tumors to the opposite side of the center, a more challenging phantom is created. Because multiple scattering objects are involved, DAS methods perform poorly in these environments, see Figure 17(c). Multitarget imaging can be misguided by numerous internal reflections caused by multiple targets. As a result, the suggested system employs DMAS-based algorithm, which rewards better coherence by multiplying individual pairs of delayed signals and combining them as a measure of coherence. A correlation process used by the DMAS results in higher contrast images than other DAS methods [33]. Multiple targets can be successfully detected using the DMAS algorithm, as shown in Figure 17(d). It is apparent from the image that the proposed system successfully detects tumors by giving them a dark red color. The slices are taken at $z = 5$ mm from the chest wall. Both x and y have ranges in meters. Table 1 shows a comparison of antennas and imaging methods for different imaging systems and the proposed system. The designed system is an effective method for using microwave imaging to detect breast cancer.

6. Conclusions

This paper presents the design, simulation, and fabrication of a lightweight, portable PLPA element loaded with metamaterials. An investigation and validation of the microwave imaging properties of the 50×40 mm² PLPA were conducted. After loading a (1×6) unit cell structure onto the radiating patch, the antenna demonstrated high gain with directional radiation patterns. Modified sensor elements are a part of the proposed MIS; the designed system has 16 antennas operating between 2 and 5 GHz. The DAS and DMAS algorithms in MATLAB are used to reconstruct the image from signals collected by the circular antenna array elements to detect breast cancer. An approach based on DMAS outperforms the DAS algorithm. With this technique, a rotation subtraction method was used for artifact removal. Metamaterial-loaded PLPA array-based MIS using the DMAS algorithm presents an excellent performance, which is why it is one of the most effective ways to detect and find cancer cells.

Data Availability

The data used to support the findings of this study are included within the article.

Conflicts of Interest

The authors declare that they have no conflicts of interest.

Acknowledgments

References

[1] S. Shin, "El cancer," 2017, https://www.aecc.es/SobreElCancer/elcancer/Paginas/Elcancer.aspx.

[2] L. Fass, "Imaging and cancer: a review," *Molecular Oncology*, vol. 2, no. 2, pp. 115–152, 2008.

[3] M. Sivasubramanian, Y. Hsia, and L. W. Lo, "Nanoparticle-facilitated functional and molecular imaging for the early detection of cancer," *Frontiers in Molecular Biosciences*, vol. 1, p. 15, 2014 þ.

[4] N. Niranjan kumar, B. S. Srikanth, S. B. Gurung et al., "A slotted UWB monopole antenna with truncated ground plane for breast cancer detection," *Alexandria Engineering Journal*, vol. 59, no. 5, pp. 3767–3780, 2020.

[5] K. Paulsen, S. Poplack, D. Li, M. Fanning, and P. Meaney, "A clinical prototype for active microwave imaging of the breast," *IEEE Transactions on Microwave Theory and Techniques*, vol. 48, no. 11, pp. 1841–1853, 2000.

[6] E. Porter, A. Santorelli, and M. Popovic, "Time-domain microwave radar applied to breast imaging: measurement reliability in a clinical setting," *Progress in Electromagnetics Research*, vol. 149, pp. 119–132, 2014.

[7] E. C. Fear, J. Bourqui, C. Curtis, D. Mew, B. Docktor, and C. Romano, "Microwave breast imaging with a monostatic radar-based system: a study of application to patients," *IEEE Transactions on Microwave Theory and Techniques*, vol. 61, no. 5, pp. 2119–2128, 2013.

[8] R. K. Amineh, M. Ravan, A. Trehan, and N. K. Nikolova, "Near-field microwave imaging based on aperture raster scanning with TEM horn antennas," *IEEE Transactions on Antennas and Propagation*, vol. 59, no. 3, pp. 928–940, 2011.

[9] S. Kwon and S. J. Lee, "Instantaneous microwave imaging with time-domain measurements for breast cancer detection," *Electronics Letters*, vol. 49, no. 10, pp. 639–641, 2013.

[10] B. J. Mohammed, A. M. Abbosh, and P. Sharpe, "Planar array of corrugated tapered slot antennas for ultrawideband biomedical microwave imaging system," *International Journal of RF and Microwave Computer-Aided Engineering*, vol. 23, no. 1, pp. 59–66, 2013.

[11] M. Z. Mahmud, M. T. Islam, and M. Samsuzzaman, "A high performance UWB antenna design for microwave imaging system," *Microwave and Optical Technology Letters*, vol. 58, no. 8, pp. 1824–1831, 2016.

[12] E. Porter, E. Kirshin, A. Santorelli, M. Coates, and M. Popovic, "Time-domain multistatic radar system for microwave breast screening," *IEEE Antennas and Wireless Propagation Letters*, vol. 12, no. 12, pp. 229–232, 2013.

[13] B. J. Mohammed, A. M. Abbosh, S. Mustafa, and D. Ireland, "Microwave system for head imaging," *IEEE Transactions on Instrumentation and Measurement*, vol. 63, no. 1, pp. 117–123, 2014.

[14] F. Foroutan and N. K. Nikolova, "Active sensor for microwave tissue imaging with bias-switched arrays," *Sensors*, vol. 18, no. 5, p. 1447, 2018.

[15] E. C. Fear and M. A. Stuchly, "Microwave breast tumor detection: antenna design and characterization," in *Proceedings of the IEEE Antennas and Propagation Society International Symposium. Transmitting Waves of Progress to the Next Millennium. 2000 Digest. Held in conjunction with: USNC/URSI National Radio Science Meeting*, vol. 2, pp. 1076–1079, Salt Lake City, UT, USA, July 2000.

[16] R. Natarajan, J. V. George, M. Kanagasabai, and A. Kumar Shrivastav, "A compact antipodal Vivaldi antenna for UWB applications," *IEEE Antennas and Wireless Propagation Letters*, vol. 14, pp. 1557–1560, 2015.

[17] M. Abbak, M. N. Akinci, M. Çayoren, and I. Akduman, "Experimental microwave imaging with a novel corrugated Vivaldi antenna," *IEEE Transactions on Antennas and Propagation*, vol. 65, no. 6, pp. 3302–3307, 2017.

[18] M. T. Islam, M. Samsuzzaman, M. T. Islam, S. Kibria, and M. J. Singh, "A homogeneous breast phantom measurement system with an improved modified microwave imaging antenna sensor," *Sensors*, vol. 18, no. 9, p. 2962, 2018.

[19] M. Fernández Pantoja, S. González García, M. A. Hernández-López, A. Rubio Bretones, and R. Gómez Martín, "Design of an ultra-broadband V antenna for microwave detection of breast tumors," *Microwave and Optical Technology Letters*, vol. 34, no. 3, pp. 164–166, 2002.

[20] T. Li, H. Zhai, L. Li, C. Liang, and Y. Han, "Compact UWB antenna with tunable band-notched characteristic based on microstrip open-loop resonator," *IEEE Antennas and Wireless Propagation Letters*, vol. 11, pp. 1584–1587, 2012.

[21] S. Hagness, A. Taflove, and J. E. Bridges, "Wideband ultralow reverberation antenna for biological sensing," *Electronics Letters*, vol. 33, no. 19, pp. 1594–1595, 1997.

[22] Z. J. Han, W. Song, and X. Q. Sheng, "Gain enhancement and RCS reduction for patch antenna by using polarization dependent EBG surface," *IEEE Antennas and Wireless Propagation Letters*, vol. 16, pp. 1631–1634, 2017.

[23] M. F. Imani, T. Sleasman, and D. R. Smith, "Two-dimensional dynamic metasurface apertures for computational microwave imaging," *IEEE Antennas and Wireless Propagation Letters*, vol. 17, no. 12, pp. 2299–2303, 2018.

[24] E. K. Saenz, K. Guven, E. Ozbay, I. Ederra, and R. Gonzalo, "Decoupling of multifrequency dipole antenna arrays for microwave imaging applications," *International Journal of Antennas and Propagation*, vol. 2010, Article ID 843624, 8 pages, 2010.

[25] S. Mukherjee, X. Shi, L. Udpa, S. Udpa, Y. Deng, and P. Chahal, "Design of a split-ring resonator sensor for near-field microwave imaging," *IEEE Sensors Journal*, vol. 18, no. 17, pp. 7066–7076, 2018.

[26] E. Porter, H. Bahrami, A. Santorelli, B. Gosselin, L. A. Rusch, and M. Popovic, "A wearable microwave antenna array for time-domain breast tumor screening," *IEEE Transactions on Medical Imaging*, vol. 35, no. 6, pp. 1501–1509, 2016.

[27] K. Zhang, Y. Yuan, X. Ding, B. Ratni, S. N. Burokur, and Q. Wu, "High efficiency metalenses with switchable functionalities in microwave region," *ACS applied materials & interfaces*, vol. 11, no. 31, pp. 28423–28430, 2019.

[28] R. A. Abdulhasan, R. Alias, K. N. Ramli, F. C. Seman, and R. A. Abd-Alhameed, "High gain CPW-fed UWB planar monopole antenna-based compact uniplanar frequency selective surface for microwave imaging," *International Journal of RF and Microwave Computer-Aided Engineering*, vol. 29, no. 8, p. e21757, 2019.

[29] A. Syed, N. Sobahi, M. Sheikh, R. Mittra, and H. Rmili, "Modified 16-quasi log periodic antenna array for microwave imaging of breast cancer detection," *Applied Sciences*, vol. 12, no. 1, p. 147, 2021.

[30] R. Carrel, "The design of the log-periodic dipole antenna," *IRE International Conventional Record*, vol. 9, no. 1, pp. 61–75, 1961.

[31] M. T. Islam, M. Samsuzzaman, S. Kibria, N. Misran, and M. T. Islam, "Metasurface loaded high gain antenna-based microwave imaging using iteratively corrected delay multiply and sum algorithm," *Scientific Reports*, vol. 9, no. 1, pp. 17317–17414, 2019.

[32] S. Kibria, M. Samsuzzaman, M. T. Islam, M. Z. Mahmud, N. Misran, and M. T. Islam, "Breast phantom imaging using iteratively corrected coherence factor delay and sum," *IEEE Access*, vol. 7, pp. 40822–40832, 2019.

[33] M. Mozaffarzadeh, A. Mahloojifar, M. Orooji, S. Adabi, and M. Nasiriavanaki, "Double-stage delay multiply and sum beamforming algorithm: application to linear-array photo-acoustic imaging," *IEEE Transactions on Biomedical Engineering*, vol. 65, no. 1, pp. 31–42, 2018.

[34] G. Kaur and A. Kaur, "Breast tissue tumor detection using "S" parameter analysis with an UWB stacked aperture coupled microstrip patch antenna having a "+" shaped defected ground structure," *International Journal of Microwave and Wireless Technologies*, vol. 12, no. 7, pp. 635–651, 2020.

[35] M. Abbak, M. Çayoren, and I. Akduman, "Microwave breast phantom measurements with a cavity-backed Vivaldi antenna," *IET Microwaves, Antennas & Propagation*, vol. 8, no. 13, pp. 1127–1133, 2014.

[36] Z. Akhter, BN. Abhijith, and M. J. Akhtar, "Hemisphere lens-loaded Vivaldi antenna for time domain microwave imaging of concealed objects," *Journal of Electromagnetic Waves and Applications*, vol. 30, no. 9, pp. 1183–1197, 2016.

[37] W. Shao, A. Edalati, T. R. McCollough, and W. J. McCollough, "A time-domain measurement system for UWB microwave imaging," *IEEE Transactions on Microwave Theory and Techniques*, vol. 66, no. 5, pp. 2265–2275, 2018.

[38] S. M. Salvador, E. C. Fear, M. Okoniewski, and J. R. Matyas, "Exploring joint tissues with microwave imaging," *IEEE Transactions on Microwave Theory and Techniques*, vol. 58, no. 8, pp. 2307–2313, 2010.

[39] M. T. Islam, M. Z. Mahmud, M. T. Islam, S. Kibria, and M. Samsuzzaman, "A low cost and portable microwave imaging system for breast tumor detection using UWB directional antenna array," *Scientific Reports*, vol. 9, no. 1, pp. 15491–13, 2019.

[40] H. Song, S. Sasada, T. Kadoya et al., "Detectability of breast tumor by a hand-held impulse-radar detector: performance evaluation and pilot clinical study," *Scientific Reports*, vol. 7, no. 1, pp. 16353–16411, 2017.

[41] M. Samsuzzaman, M. T. Islam, A. S. Shovon, R. I. Faruque, and N. Misran, "A 16-modified antipodal Vivaldi antenna array for microwave-based breast tumor imaging applications," *Microwave and Optical Technology Letters*, vol. 61, no. 9, pp. 2110–2118, 2019.